Analytical and Bioanalytical Chemistry
https://doi.org/10.1007/s00216-021-03203-z

RESEARCH PAPER

Novel voltammetric tumor necrosis factor-alpha (TNF-α) immunosensor based on gold nanoparticles involved in thiol-functionalized multi-walled carbon nanotubes and bimetallic Ni/Cu-MOFs

Mehmet Lütfi Yola[1] · Necip Atar[2]

Received: 4 January 2021 / Revised: 22 January 2021 / Accepted: 27 January 2021

Abstract

TNF-α, as a pro-inflammatory cytokine, regulates some physiological and pathological courses. TNF-α level increases in some important diseases such as cancer, arthritis, and diabetes. In addition, it displays an important function in Alzheimer's and cardiovascular diseases. Herein, a novel, sensitive, and selective voltammetric TNF-α immunosensor was prepared by using gold nanoparticles involved in thiol-functionalized multi-walled carbon nanotubes (AuNPs/S-MWCNTs) as sensor platform and bimetallic Ni/Cu-MOFs as sensor amplification. Firstly, the sensor platform was developed on glassy carbon electrode (GCE) surface by using mixture of thiol-functionalized MWCNTs (S-MWCNTs) and AuNPs. Then, capture TNF-α antibodies were conjugated to sensor platform by amino-gold affinity. After capture TNF-α antibodies' immobilization, a new-type voltammetric TNF-α immunosensor was developed by immune reaction between AuNPs/S-MWCNTs immobilized with primer TNF-α antibodies and bimetallic Ni/Cu-MOFs conjugated with seconder TNF-α antibodies. The prepared TNF-α immunosensor was characterized by transmission electron microscopy (TEM), scanning electron microscopy (SEM), x-ray diffraction (XRD) method, x-ray photoelectron spectroscopy (XPS), atomic force microscopy (AFM), thermogravimetric analysis, Fourier transform infrared spectroscopy (FTIR), cyclic voltammetry (CV), and electrochemical impedance spectroscopy (EIS). A linearity range of 0.01–1.0 pg mL^{-1} and a low detection limit of 2.00 fg mL^{-1} were also obtained for analytical applications.

Keywords Tumor necrosis factor-alpha · Immunosensor · Voltammetry · Bimetallic Ni/Cu-MOFs · Composite

Introduction

Cytokines having low molecular weight are significant biomarkers and they are produced by distinct cells relating to immune system [1, 2]. Several cytokines can be utilized as imaging biomarker for the immune system description and illnesses prediction. Cytokines are investigated as two groups: (i) pro-inflammatory (TNF-α, IL-1, IL-2, IL-6, IL-8) and anti-inflammatory (IL-4, IL-10, IL-13). Pro-inflammatory cytokines, which are formed by macrophages, corresponded to inflammatory immune reactions and pathological pain operations [3]. TNF-α as pro-inflammatory cytokine can affect various aspects of the immune reaction. TNF-α amount is initially low. Nonetheless, due to many diseases such as rheumatoid arthritis, cancer, and diabetes, its concentration increases [4–9]. Hence, the sensitive and selective recognition methods' preparation for important biomarkers is currently significant in terms of clinical diagnosis [10]. Conventional methods such as ELISA [11], enzyme-linked immunosorbent [12], and antibody [13] assays were presented for cytokines' determination. In addition, some immunosensors such as fluorescence [14], surface plasmon resonance [15], and silicon photonic resonator [16] were reported for target cytokine analysis. A non-labeled localized SPR cytokine biosensor was also fabricated for TNF-α detection in plasma samples [17]. Nonetheless, these techniques have some problems

✉ Mehmet Lütfi Yola
mlutfi.yola@hku.edu.tr

[1] Faculty of Health Sciences, Department of Nutrition and Dietetics, Hasan Kalyoncu University, 27000 Gaziantep, Turkey

[2] Faculty of Engineering, Department of Chemical Engineering, Pamukkale University, 20160 Denizli, Turkey

Published online: 05 February 2021

such as high costly equipment, slowness, and the need of experienced staff. Up to now, the general detection method for cytokine determination has been electrochemical immunosensors. New-type electrochemical immunosensors/sensors have important advantages such as high sensitivity, selectivity, shorter analysis time, and lower costs [18–24]. Generally, the electrochemical immunosensors for cytokine detection are investigated in two groups: (i) sandwich type with label and (ii) label-free. Especially, sandwich-type immunosensors are widely utilized due to highly sensitivity and stable sensor signals [25]. In this sandwich-type immunosensors, the capture antibody is conjugated to sensor platform such as glassy carbon electrode and the analyte (target) antigen sandwiched between the capture and seconder antibodies. In addition, any nanomaterial/composite is an important factor to improve the sensitivity and the detection limit [26]. For instance, CdTe QDs and polymer-functionalized silica hybrid nanostructure as a label-based electrochemical immunosensor were prepared for TNF-α quantification. The electropolymerization was carried out on gold electrode surface and a linearity range of 0.01–100.0 ng mL^{-1} and a low detection limit of 3.00 pg mL^{-1} were obtained [27]. In other example, a sandwich-type electrochemical immunosensor was developed for interleukin-1β and TNF-α detections by using functionalized double-walled carbon nanotubes (DWCNTs) and poly-HRP-streptavidin conjugates. A linearity range of 1.0–200.0 ng mL^{-1} and a low detection limit of 0.85 pg mL^{-1} were calculated [28].

Carbon nanotubes as sensor platform have good conductivity and perfect chemical stability [29]. Especially, due to their acceleration ability of electron transfer on electrochemical electrode surface and large surface area [30], carbon nanotubes are used in construction of fast electrochemical sensors [31]. In addition, the composites of carbon nanotubes and gold nanoparticles can be utilized as catalyst because of stability and the enhanced conductivity.

Currently, metal-organic frameworks (MOFs) can be used frequently owing to pore structure and specific surface area [32]. These characteristic properties make MOFs important sensor amplifications in the field of electrochemical applications and energy storage [33, 34]. In this case, MOF-based electrode materials have also been applied for detection cancer cell and biomolecule [35, 36]. Especially, MOFs are utilized for the determination of important substances [37] due to their high reactivity [38]. In addition, due to perfect structural properties, bimetallic MOFs can start to take great interest. Especially, bimetallic MOFs' higher reactivity in comparison with monometallic MOFs owing to distinct metal ions' combination and the synergistic effect provides bimetallic MOFs more applicable on sensor technology [39]. Bimetallic MOFs' rich metal active sites can also facilitate the electron transfer on electrode surface [40]. Hence, bimetallic MOFs have important potential on clinical applications.

Herein, a new sandwich-type voltammetric immunosensor based on gold nanoparticles involved in thiol-functionalized multi-walled carbon nanotubes and bimetallic Ni/Cu-MOFs for TNF-α detection was developed. The developed immunosensor demonstrated a detection limit of 2.00 fg mL^{-1} and perfect selective responses in the presence of other substances. Finally, a new opportunity can be created for a clinical application by using this sandwich-type voltammetric immunosensor.

Materials and methods

Materials

Antigen TNF-α; capture antibody1-TNF-α (primer, anti-TNF-α-Ab_1); detection antibody2-TNF-α (seconder, anti-TNF-α-Ab_2); interleukin-1 (IL-1), IL-2, IL-4, IL-6, IL-10; bovine serum albumin (BSA); MWCNTs (25–30 nm in diameter and 1.0–5.0 μm in length); 4-aminothiophenol (4-ATP); gold (III) chloride trihydrate ($HAuCl_4 \cdot 3H_2O$); $Na_3C_6H_5O_7 \cdot 2H_2O$, 1-ethyl-3-(3-dimethylaminopropyl) carbodiimide (EDC); N-hydroxysuccinimide (NHS); 2,3,6,7,10,11-hexaaminohexatyl hydrogen hexachloride (HATP·6HCl); $NiCl_2.6H_2O$; and $CuSO_4 \cdot 5H_2O$ were purchased from Sigma-Aldrich. Phosphate buffer solution (PBS, 0.1 M, pH 7.0) as supporting electrolyte and dilution buffer was also utilized.

Instrumentation

SEM and XRD images were obtained by using ZEISS EVO 50 SEM analytical microscopy and Rigaku X-ray diffractometer, respectively. JEOL 2100 TEM was used for TEM measurement. XPS analysis was carried out by using PHI 5000 Versa Probe. Gamry Reference 600 workstation (Gamry, USA) was utilized for differential pulse voltammetry (DPV), CV, and EIS measurements. FTIR measurements were obtained by Bruker Tensor 27 FT-IR with DTGS detector.

MWCNT functionalization

MWCNT (50.0 mg) was added into $HNO_3 + H_2SO_4$ (3:1) (v/v) solution under strong stirring for 12 h. The dispersion was filtered and washed with pure water up to pH 6.5–7.0 to open MWCNTs' ends. The carboxylated MWCNT was dried at 100 °C for 12 h. Hence, the carboxylated MWCNT was used for AuNP/S-MWCNT composite preparation [41].

Preparation of AuNPs and AuNP/S-MWCNT composite

AuNPs having the mean diameters of 20–22 nm were prepared by using $Na_3C_6H_5O_7 \cdot 2H_2O$ as reducing agent and

$HAuCl_4 \cdot 3H_2O$ as precursor agent in harmony with literature [42].

After preparation of carboxylated MWCNT solution (0.1 mg mL^{-1}) in ethanol, the solution was interacted with the mixture of NHS (50.0 mM, 10.0 mL) and EDC (50.0 mM, 10.0 mL) to activate carboxylic groups of MWCNTs for 12 h. Then, the activated MWCNTs was added into 4-ATP solution (1.0 mM) at (1:1) (v/v) and self-assembly esterification reaction was followed during 2 h for thiol-functionalized MWCNT (S-MWCNT) synthesis. After that, the mixture of S-MWCNTs (0.2 mg mL^{-1}) and AuNPs (20.0 mg mL^{-1}) was interacted with each other at (1:1) (v/v) via sulfur-gold affinity for 20 min and the obtained AuNP/S-MWCNT was kept at 25 °C.

AuNP/S-MWCNT composite as electrochemical sensor platform with anti-TNF-α-Ab_1 and antigen TNF-α immobilizations

Firstly, AuNP/S-MWCNT composite-modified glassy carbon electrode (AuNP/S-MWCNT/GCE) was developed. For this aim, AuNP/S-MWCNT composite dispersion (20.0 μL) was dropped on the clean GCE surfaces and drying process was performed under IR lamp. Then, the first immobilization of anti-TNF-α-Ab_1 on AuNPs/S-MWCNTs/GCE was carried out by anti-TNF-α-Ab_1 dispersion (20.0 μL, 10.0 μg mL^{-1}) dropping on electrode surface via amino-gold affinity at 37.0 °C for 45 min [43, 44]. After that, the blockage treatment of anti-TNF-α-Ab_1/AuNPs/S-MWCNTs/GCE was carried out by BSA (2.0% w/v) at 37.0 °C for 45 min to remove non-specific interactions. After washing with pH 7.0, 0.1 M PBS, various antigen TNF-α amounts were immobilized on anti-TNF-α-Ab_1/AuNPs/S-MWCNTs/GCE for 45 min at 37 °C and TNF-α/anti-TNF-α-Ab_1/AuNP/S-MWCNT/GCE was created. Lastly, the developed TNF-α/anti-TNF-α-Ab_1/AuNP/S-MWCNT/GCE was washed with 0.1 M PBS (pH 7.0) to eliminate unbounded TNF-α proteins.

Synthesis of Ni-MOFs, Cu-MOFs, Ni/Cu-MOFs, and Ni/Cu-MOFs as signal amplification with anti-TNF-α-Ab_2 conjugation

$NiCl_2.6H_2O$ aqueous solution (0.01 mmol), $NH_3 \cdot H_2O$ (0.5 mL), and HATP·6HCl aqueous solution (0.01 mmol) were mixed at 25.0 °C under strong stirring for 30 min. After that, the prepared solution was transferred into Teflon autoclave at 100 °C during 5 h. After cooling treatment at 25.0 °C, the centrifugation treatment provided a green precipitation (Ni-MOFs). Ni-MOF was washed with ethanol and dried at 50.0 °C for 6 h. For Cu-MOF preparation, the same protocol was applied to use the starting chemicals such as $CuSO_4 \cdot 5H_2O$ aqueous solution (0.01 mmol), $NH_3 \cdot H_2O$ (0.5 mL), and HATP·6HCl aqueous solution (0.01 mmol).

After the preparation of Ni-MOF (10.0 mg) dispersion in ethanol under strong stirring for 20 min at 25.0 °C, $CuSO_4 \cdot 5H_2O$ (2.5 mg) was dissolved in ethanol during 10 min and slowly added into Ni-MOF dispersion under stirring for 30 min. Then, the prepared mixture was transferred into Teflon autoclave at 100 °C during 5 h and cooled down to 25.0 °C. After centrifugation treatment, the obtained product was tagged as Ni/Cu-MOFs (4:1). After preparation of anti-TNF-α-Ab_2 (20.0 μL, 10.0 μg mL^{-1}), the detection antibody could be conjugated to Ni/Cu-MOFs (4:1) via electrostatic and π-π stacking interactions between anti-TNF-α-Ab_2 and Ni/Cu-MOF (4:1) dispersions [45]. Then, the centrifugation treatment was performed at 10000 rpm, and Ni/Cu-MOF (4:1) conjugated to anti-TNF-α-Ab_2 (Ni/Cu-MOF/anti-TNF-α-Ab_2) was stored in pH 7.0, 0.1 M PBS.

Electrochemical measurements

In this study, the antibody-antigen interactions between Ni/Cu-MOFs/anti-TNF-α-Ab_2 and TNF-α/anti-TNF-α-Ab_1/AuNPs/S-MWCNTs/GCE develop a novel voltammetric TNF-α immunosensor. After the incubation of Ni/Cu-MOFs/anti-TNF-α-Ab_2 solution (20.0 μL, 10.0 mg mL^{-1}) on TNF-α/anti-TNF-α-Ab_1/AuNPs/S-MWCNTs/GCE during the immune reaction of 30 min, the prepared voltammetric immunosensor (Ni/Cu-MOFs/anti-TNF-α-Ab_2/TNF-α/anti-TNF-α-Ab_1/AuNPs/S-MWCNTs/GCE) was stored in pH 7.0, 0.1 M PBS. Supporting electrolyte including pH 7.0, 0.1 M PBS (2.0 mL) containing 1.0 mM H_2O_2 solution was prepared for voltammetric measurements at + 0.40 V. H_2O_2 as a redox probe was selected owing to its usage in biomolecules' medical diagnosis [25, 46]. Before the voltammetric measurements, argon gas (99.999%) was passed to remove dissolved oxygen for 10 min. In addition, the voltammograms were recorded without pressure fluctuations at 25 °C in an enclosed cabinet to prevent from external environmental influences.

Sample preparation

TNF-α-free plasma samples were supplied from Hacettepe University, Blood Bank, in Turkey. Sample preparation protocol was explained in detail in Supplementary Information (ESM) [47].

Results and discussion

Detection principle of voltammetric TNF-α immunosensor

Scheme 1 shows preparation procedure of voltammetric TNF-α immunosensor in this study. The voltammetric

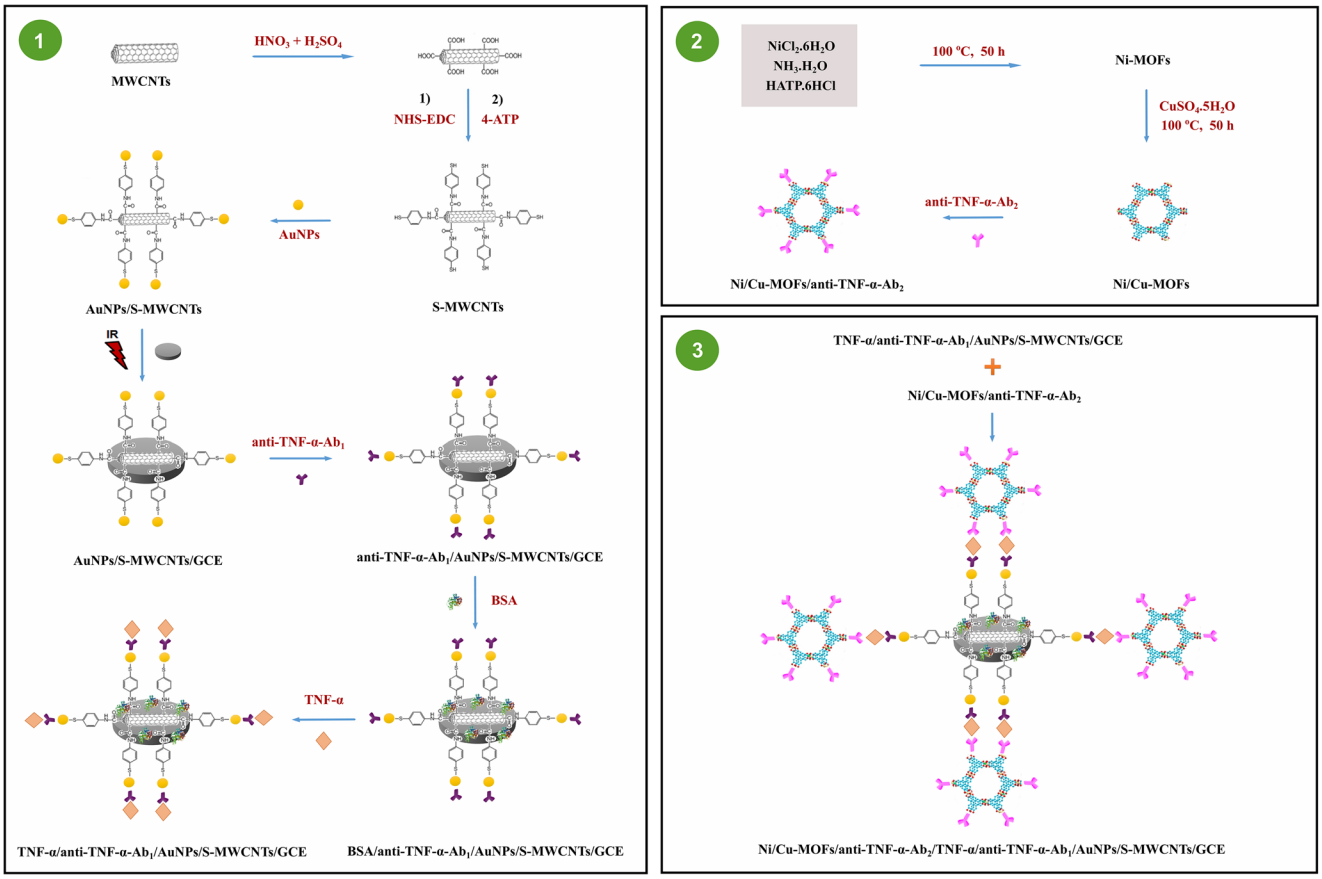

Scheme 1 Preparation procedure of voltammetric TNF-α immunosensor

immunosensor for antigen TNF-α recognition was developed based on gold nanoparticles involved in thiol-functionalized multi-walled carbon nanotubes as sensor platform and bimetallic Ni/Cu-MOF as signal amplification. Firstly, the prepared electrochemical sensor platform has two purposes as the formation of binding sites for capture antibody1-TNF-α and conductivity enhancement on electrode surface. Secondly, owing to porosity and large internal surface of bimetallic MOFs [48, 49], seconder antibody2-TNF-α easily conjugated to bimetallic Ni/Cu-MOFs via π-π and electrostatic interactions, and thus, the electrochemical performance can be improved.

Characterizations of AuNPs/S-MWCNs as sensor platform

Firstly, FTIR spectra (Fig. 1A) were recorded to confirm the formations of carboxylated MWCNTs and thiol-functionalized MWCNTs. Spectrum a demonstrated the stretching vibrations of –C=O at 1721 cm^{-1} and –OH at 3418 cm^{-1}. In addition, the covalently attached 4-ATP to carboxylated MWCNTs was verified on spectrum b. The observed stretching vibrations of –C=O at 1721 cm^{-1} on spectrum a were observed at 1735 cm^{-1} on spectrum b. This shift confirmed 4-ATP's covalent attachment. Absorption bands at 1619 cm^{-1}, 1359 cm^{-1}, 2575 cm^{-1}, and 3648 cm^{-1} also corresponded to aromatic –C=C– stretching, C–H bending, –S–H stretching, and –N–H stretching, respectively. Figure 1B and C demonstrated TEM images of carboxylated MWCNTs and AuNP/S-MWCNT composite, respectively. According to Fig. 1B, the typical nanotube morphology was obtained. However, after the formation of AuNP/S-MWCNT composite, the homogeneous distributions of AuNPs as spherical shapes with a mean diameter of 20–22 nm on S-MWCNTs' outside were observed on Fig. 1C.

The confirmation of AuNP/S-MWCNT composite formation was also provided by XPS (ESM Fig. S1A) and XRD (ESM Fig. S1B) characterizations. According to the deconvolution spectra of C_{1s}, the peaks at 287.2, 285.1, and 284.2 eV were attributed to –CONH, C–O or C–N, and C–H, respectively [50]. In addition, the peaks at 398.1 eV and 401.2 eV on N_{1s} narrow region spectra corresponded to the formed amide's N–H groups via esterification and N-H groups in unreacted 4-ATP, respectively. The observed peaks at 164.1 and 163.5 eV confirmed the sulfur presence on AuNP/S-MWCNT composite, indicating Au-S bond [51]. Finally, the Au presence was confirmed to observe Au $4f_{7/2}$ peak at 83.8 eV and the presence of unreacted AuNPs was verified at 88.1 eV. Thus, AuNP/S-MWCNT composite was

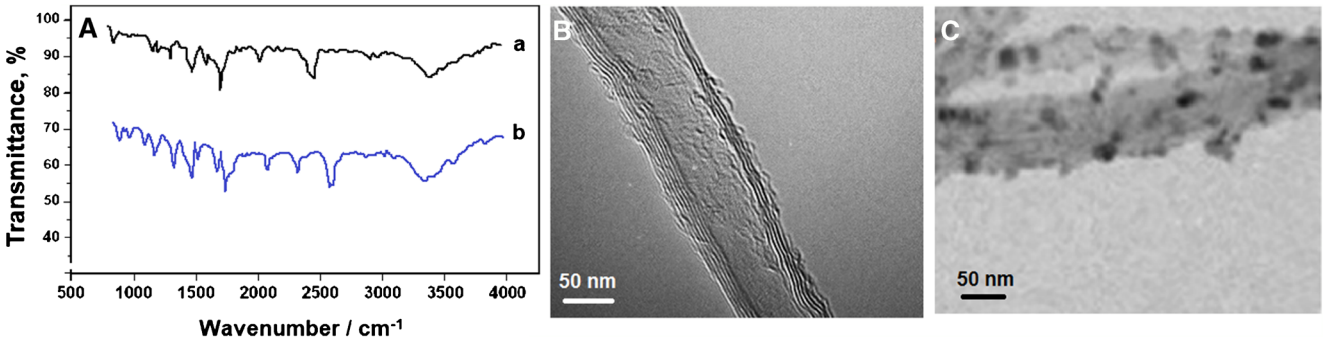

Fig. 1 (A) FTIR spectra of (a) carboxylated MWCNTs and (b) thiol-functionalized MWCNTs, TEM images of (B) carboxylated MWCNTs, and (C) AuNP/S-MWCNT composite

successfully prepared as electrochemical immunosensor platform. According to XRD spectra, (002) and (101) planes corresponding to 2θ = 25.9° and 43.95° confirmed the presence of MWCNTs [52], and (111), (200), and (220) planes attributing to 2θ = 38.3°, 45.1°, and 63.9° verified AuNP formation on composite [50].

Characterizations of Ni-MOFs, Cu-MOFs, and Ni/Cu-MOFs

According to Fig. 2A, XRD peak locations of bimetallic Ni/Cu-MOFs coherent to that of Ni-MOFs and Cu-MOFs were observed at 2θ = 4.5°, 9.3°, 12.3°, 16.5°, and 27.3° [53], indicating Ni/Cu-MOFs, Ni-MOFs, and Cu-MOFs having similar crystal structures. XRD peaks at 4.5°, 9.3°, and 27.3° also corresponded to (100), (200), and (001) plane of MOFs, respectively. Secondly, FTIR spectra (Fig. 2B) demonstrated Ni-MOFs, Cu-MOFs, and Ni/Cu-MOFs' similar chemical structures. The absorption bands at 3421 cm^{-1} were attributed to benzene ring's amino groups ($–NH_2$), and the peaks at 2921 cm^{-1}, 2852 cm^{-1}, and 1402 cm^{-1} corresponded to hydrocarbon (–CH) bonds' out-of-plane and in-plane bending on benzene. The vibrations of benzene ring's –C=C– groups and carbon-nitrogen bonds between amino groups and benzene ring's –CN groups were observed at 1625 cm^{-1} and 1115 cm^{-1}, respectively [54]. According to XPS spectra (Fig. 2C), the binding energies attributing to O1s, N1s, and C1s were observed at 533.12 eV, 398.92 eV, and 285.03 eV,

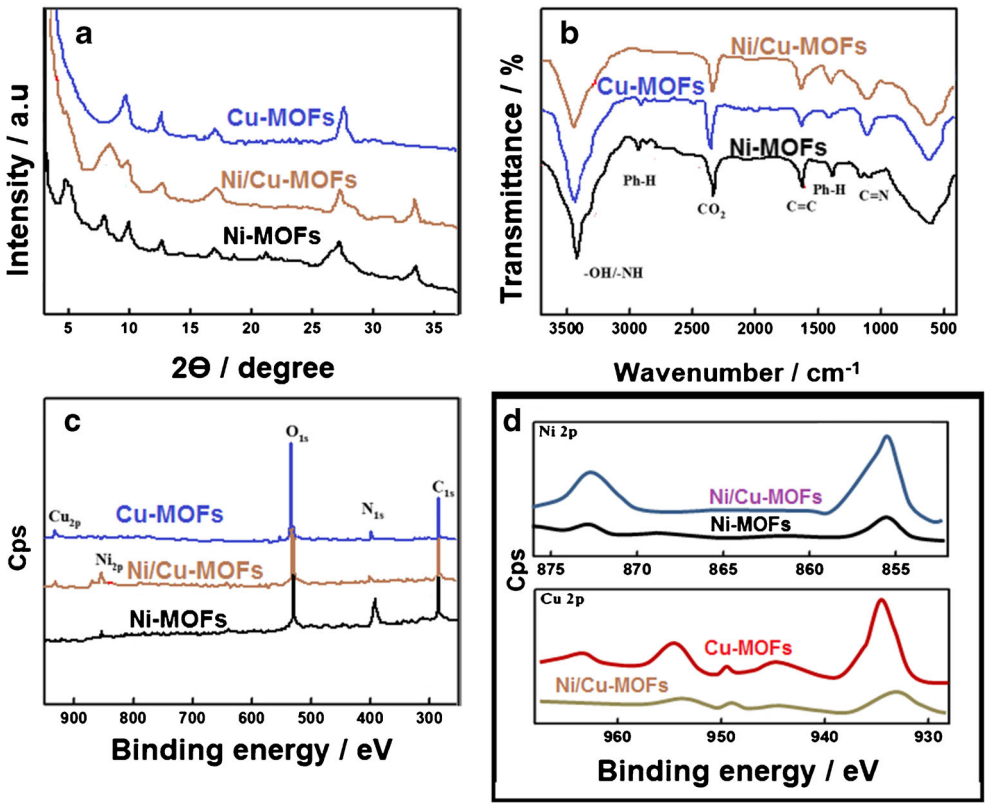

Fig. 2 (A) XRD spectra, (B) FTIR spectra, (C) XPS spectra of Ni-MOFs, Cu-MOFs, and Ni/Cu-MOFs (4:1), and (D) high-resolution XPS spectra of Ni2p in Ni-MOFs and Ni/Cu-MOFs (4:1) and Cu2p in Cu-MOFs and Ni/Cu-MOFs (4:1)

respectively. In addition, the peaks at 856.02 eV and 872.11 eV relating to Ni2p and the peaks at 935.13 eV relating to Cu2p were obtained. These peaks confirmed the participation of Ni ions and Cu ions into coordination for Ni/Cu-MOF formation. Finally, the high-resolution XPS spectra (Fig. 2D) of Ni2p and Cu2p confirmed the successful synthesis of bimetallic Ni/Cu-MOFs. Ni2p's binding energy increased by 0.33 eV in comparison with that of Ni-MOFs and Cu2p's binding energy decreased by 1.34 eV in comparison with that of Cu-MOFs. The results showed that the electron transfer between Ni and Cu ions occurred on aromatic ring of HATP, indicating coupling effect of Ni-Cu. Due to ionic state interaction, the charge transfer between Ni and Cu ions increased, showing the electrical conductivity improvement of bimetallic Ni/Cu-MOFs. The better electron acceptable ability of Cu ions in comparison with Ni ions causing the easy tendency of electron cloud towards Cu ions provided a decrease in Cu2p's binding energy and an increase in Ni2p's binding energy.

SEM image (Fig. 3A) of Ni/Cu-MOFs demonstrated that dense, tiny contact sites and large surface area having sheet-like fold structure were obtained in comparison with Ni-MOFs (Fig. 3B) and Cu-MOFs (Fig. 3C). This situation confirmed the important improvement on specific surface area of Ni/Cu-MOFs and easy modification of surfaces. In addition, the cross-sectional morphologies of Ni/Cu-MOFs (Fig. 3D) and Ni-MOFs (Fig. 3E) were obtained. According to the cross-sectional morphologies, Ni/Cu-MOFs' film thickness was about 496 nm, which was almost the same order in comparison with Ni-MOFs (507 nm). In conclusion, the rougher and more tiny protrusions were observed on Ni/Cu-MOFs' structure. AFM was utilized to show the roughness changes of Ni/Cu-MOFs and Ni-MOFs (ESM Fig. S2A and ESM Fig. S2B). Thus, we can say that Ni/Cu-MOFs had greater surface roughness than that of Ni-MOFs. In addition, the contact angle method (ESM Fig. S2C, D, and E) confirmed the hydrophilicity's improvement of Ni/Cu-MOFs. The contact angle value (126.47°) of Ni-MOFs was bigger than that of Ni/Cu-MOFs (103.37°), indicating an increase on the hydrophilicity property of Ni/Cu-MOFs. Nonetheless, Ni/Cu-MOFs/anti-TNF-α-Ab_2's contact angle value significantly decreased to about 46.71° owing to anti-TNF-α-Ab_2's conjugation providing the improvement of hydrophilic property.

In addition, the uniform distribution of Ni and Cu elements in Ni/Cu-MOFs was shown in Fig. S3 (see ESM). Hence, the successful preparation of Ni/Cu-MOFs was presented in this study. Figure S4 (see ESM) also showed thermogravimetric analysis for thermal stability of Ni/Cu-MOFs (4:1). The decomposition temperature (266 °C) of Ni/Cu-MOFs (4:1) was lower than that of Ni-MOFs (306 °C). Nonetheless, it was higher than that of Cu-MOFs (229 °C). This difference was owing to the higher chemical activity resulted from synergistic effect in bimetallic Ni/Cu-MOFs [55]. The surface morphologies of Ni/Cu-MOFs with various molar ratios were investigated on Fig. S5 (see ESM). The surface morphologies of Ni/Cu-MOFs (1:4) (ESM Fig. S5A) and Ni/Cu-MOFs (1:1) (ESM Fig. S5B) were similar to Cu-MOFs. Especially, due to precipitation between Cu ions and HATP, the formation of dense MOF films becomes harder. Nonetheless, the dense MOF formation as stacked structure was observed on Ni/Cu-MOFs (4:1) (ESM Fig. S5C) and Ni/Cu-MOFs (8:1) (ESM Fig. S5D). Hence, Ni/Cu-MOFs (4:1) as signal amplification

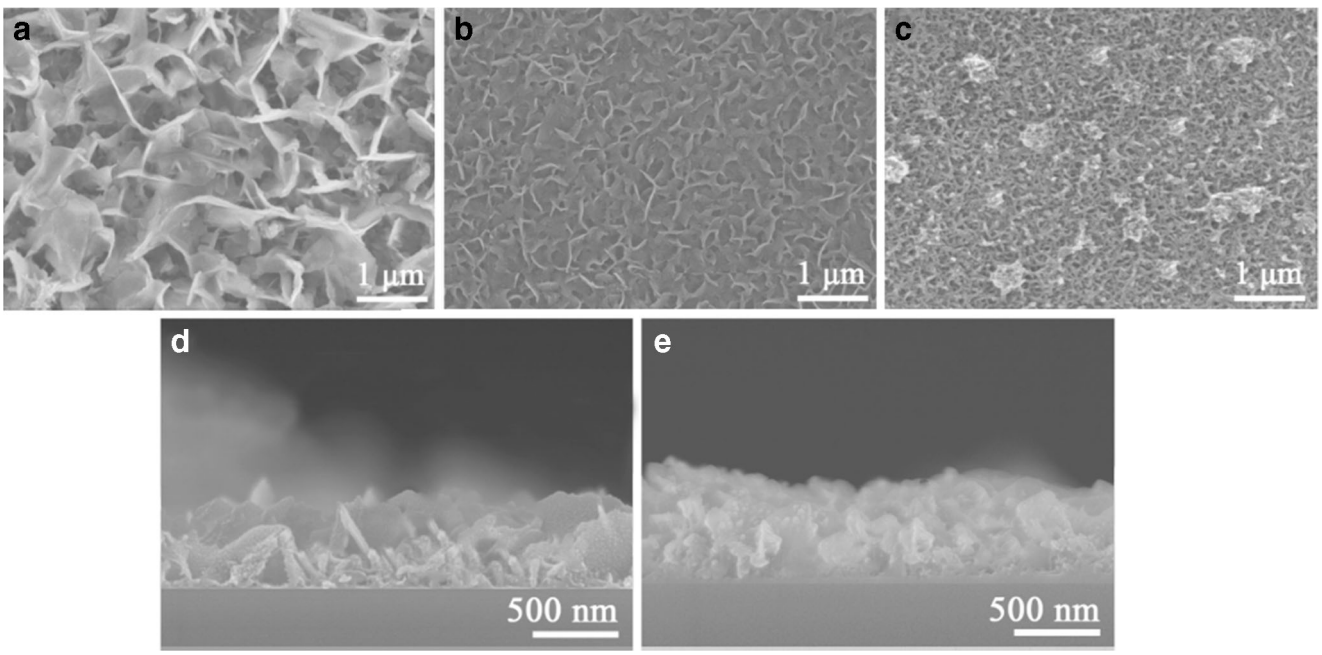

Fig. 3 SEM images of (A) Ni/Cu-MOFs (4:1), (B) Ni-MOFs, and (C) Cu-MOFs. Cross-section images of (D) Ni/Cu-MOFs (4:1) and (E) Ni-MOFs

was utilized for electrochemical immunosensor development. Figure S5E (see ESM) demonstrated some cloudy clusters on Ni/Cu-MOFs (4:1), confirming conjugation of anti-TNF-α-Ab_2 on Ni/Cu-MOFs (4:1). Lastly, SEM image of Ni/Cu-MOF/anti-TNF-α-Ab_2/TNF-α/anti-TNF-α-Ab_1/AuNP/S-MWCNT was presented (ESM Fig. S5F). According to Fig. S5F, owing to more antibody-antigen interactions between Ni/Cu-MOFs/anti-TNF-α-Ab_2 and TNF-α/anti-TNF-α-Ab_1/AuNPs/S-MWCNTs, a bigger spherical size and more agglomeration in comparison with Ni/Cu-MOFs/anti-TNF-α-Ab_2 were observed, confirming a successful immune reaction.

Electrochemical characterizations of proposed voltammetric immunosensor

Electrochemical characterizations of prepared sensor platform (TNF-α/anti-TNF-α-Ab_1/AuNPs/S-MWCNTs/GCE) was progressively investigated in 1.0 mM $[Fe(CN)_6]^{3-}$ containing 0.1 M KCl by CV and EIS. The certain anodic and cathodic peaks were observed by using bare GCE (curve a of Fig. 4A). These anodic and cathodic peaks appeared to be more pronounced and severe by using carboxylated MWCNTs/GCE owing to the electrical conductivity and facilitation of electron transfer [42] (curve b of Fig. 4A). Even the enhanced anodic and cathodic peak intensities were obtained at AuNPs/S-MWCNTs/GCE (curve c of Fig. 4A) due to the synergistic effect between MWCNTs and AuNPs [56] and good electrocatalytic activity and active surface area of AuNPs [57]. After that, the immobilization of capture anti-TNF-α-Ab_1 was verified by seeing a significant decrease in peak intensities and electron transfer prevention on anti-TNF-α-Ab_1/AuNPs/S-MWCNTs/GCE (curve d of Fig. 4A). In addition, the peak signals further decreased on curve e of Fig. 4A, indicating BSA's blocking effect on electron transfer. Finally, the immobilization of antigen TNF-α on sensor platform (curve f of Fig. 4A) was more obstructive to electron transfer in comparison with curve e of Fig. 4A. Thus, we can say that CV results showed that proteins of capture, antigen, seconder, and BSA could readily bond to carbon electrode surface modified with AuNP/S-MWCNT composite.

Secondly, EIS measurements were progressively performed for electrochemical investigation of proposed voltammetric immunosensor in 1.0 mM $[Fe(CN)_6]^{3-}$ containing 0.1 M KCl. EIS graph of bare GCE was demonstrated on curve a of Fig. 4B. Then, the values of resistance were gradually reduced by using carboxylated MWCNTs/GCE (curve b of Fig. 4B) and AuNPs/S-MWCNTs/GCE (curve c of Fig. 4B). Due to capture anti-TNF-α-Ab_1 immobilization, the electrochemical conductivity on electrode surface decreased, indicating the resistance increase on electrode (curve d of Fig. 4B). Lastly, the values of electrochemical conductivity gradually decreased by BSA's blocking effect (curve e of Fig. 4B) and obstructive effect of antigen TNF-α on electron transfer (curve f of Fig. 4B). Thus, according to CV and EIS measurements, the successful construction of electrochemical sensor platform was performed for novel TNF-α recognition.

In order to demonstrate high electrocatalytic activity of Ni/Cu-MOFs (4:1) as signal amplification for H_2O_2 detection, three immunosensors such as anti-TNF-α-Ab_2/TNF-α/anti-TNF-α-Ab_1/AuNPs/S-MWCNTs/GCE, Ni-MOFs/anti-TNF-α-Ab_2/TNF-α/anti-TNF-α-Ab_1/AuNPs/S-MWCNTs/GCE, and Ni/Cu-MOFs/anti-TNF-α-Ab_2/TNF-α/anti-TNF-α-Ab_1/AuNPs/S-MWCNTs/GCE were prepared for 1.0 mM H_2O_2 in pH 7.0, 0.1 M PBS (ESM Fig. S6). Firstly, the prepared sensor platforms (anti-TNF-α-Ab_1/AuNPs/S-MWCNTs/GCE) were incubated with antigen TNF-α (0.20 pg mL^{-1}) for 45 min at 37 °C. Then, the prepared TNF-α/anti-TNF-α-Ab_1/AuNPs/S-MWCNTs/GCE was put on an immune reaction in the presence of anti-TNF-α-Ab_2, Ni-MOFs/anti-TNF-α-Ab_2, and Ni/Cu-MOFs/anti-TNF-α-Ab_2, respectively. The whole immunosensors were tested in 1.0 mM H_2O_2 in pH 7.0, 0.1 M PBS (curve b), and in absence of H_2O_2 (curve a). According to curve b of Fig. S6A (see ESM), seconder anti-TNF-α-Ab_2 incubated to sensor platform demonstrated a small signal for 1.0 mM H_2O_2 at about + 0.40 V. In addition, the obtained peak signal on Ni-MOFs/anti-TNF-α-Ab_2 incubated to sensor platform (ESM Fig. S6B) was smaller than that of Ni/Cu-MOFs/anti-TNF-α-Ab_2 incubated to sensor platform (ESM Fig. S6C) in the presence of 1.0 mM H_2O_2 in pH 7.0, 0.1 M PBS. Owing to the better

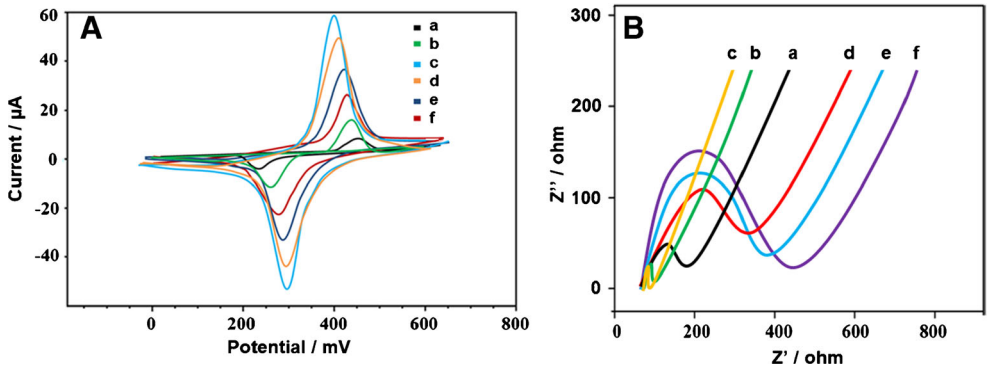

Fig. 4 (A) Cyclic voltammograms and (B) EIS responses at (a) bare GCE, (b) carboxylated MWCNTs/GCE, (c) AuNPs/S-MWCNTs/GCE, (d) anti-TNF-α-Ab_1/AuNPs/S-MWCNTs/GCE, (e) BSA/anti-TNF-α-Ab_1/AuNPs/S-MWCNTs/GCE, (f) TNF-α/anti-TNF-α-Ab_1/AuNPs/S-MWCNTs/GCE (scan rate of 100 mV s^{-1})

electrical conductivity, large surface area and rich electroactive sites of Ni/Cu-MOFs in comparison with Ni-MOFs, the more efficient adsorption and reaction surface for target proteins can be provided. Finally, the synergistic effect between Ni and Cu ions makes the developed immunosensor feasible for real-time tumor necrosis factor-alpha detection with high selectivity and sensitivity [39]. According to the obtained results, the significant improvements on immunosensor sensitivity were observed by using Ni/Cu-MOFs (4:1) as signal amplification.

Optimization for voltammetric measurements

The effects of pH, immune reaction time, H_2O_2, and Ni/Cu-MOFs/anti-TNF-α-Ab_2 solution concentrations were evaluated in detail on Fig. S7 (see ESM).

Linearity range

By using the developed voltammetric TNF-α immunosensor, the obtained voltammograms (Fig. 5) and linearity relation between immunosensor signals and TNF-α concentrations was found to be y (μA) = 54.602x (pg mL^{-1}) − 0.0398 (inset of Fig. 5). The quantification limit (LOQ) and detection limit (LOD) were calculated as 0.01 pg mL^{-1} and 2.00 fg mL^{-1}, respectively, by equations below:

$$\mathrm{LOQ} = 10.0\ S/m \quad (1)$$

$$\mathrm{LOD} = 3.3\ S/m \quad (2)$$

where S is standard deviation of intercept and m is slope of calibration equation. According to Table 1, favorable sensitivity and selectivity were observed towards TNF-α by developed voltammetric TNF-α immunosensor in comparison with previous studies. Due to the improved conductivity resulted from synergistic effect between Ni and Cu ions and rich electroactive sites of bimetallic MOFs, the conjugation of seconder antibody2-TNF-α to bimetallic Ni/Cu-MOFs was easily provided. In addition, the preparation procedure including AuNP/S-MWCNT composite and bimetallic Ni/Cu-MOFs was low in cost and waste generation was minimal, presenting an environmentally friendly immunosensor. Furthermore, the analysis time was shorter in comparison with the other methods. In conclusion, the presented voltammetric TNF-α immunosensor can be used for more complex clinical applications.

Recovery

The calculated recovery values, relating to the prepared antigen plasma samples in the section "Sample preparation" of Supplementary Data, were close to 100.00% (ESM Table S1). According to Table S1, a novel TNF-α immunosensor having high selectivity was presented in this study. Moreover, to demonstrate the immunosensor's high selectivity, standard addition method was applied to plasma samples. Calibration equation belonging to standard addition method was found as y (μA) = 54.686x (pg mL^{-1}) − 0.472. The close slope values between direct calibration and standard

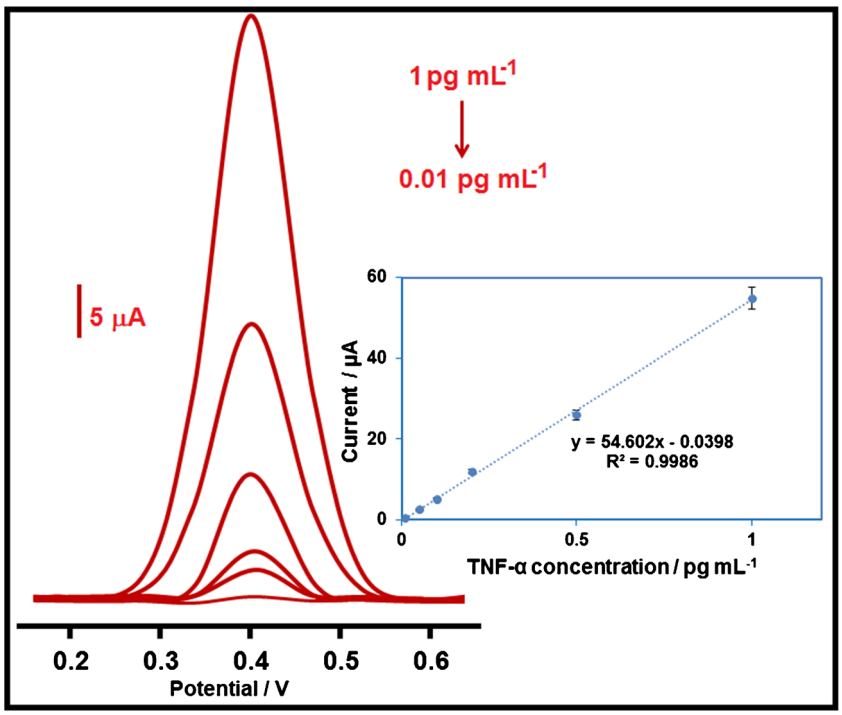

Fig. 5 Concentration effect (from 0.01 to 1.0 pg mL^{-1} TNF-α) on immunosensor signals. Inset: Calibration curve for voltammetric TNF-α immunosensor

Table 1 Comparison of voltammetric TNF-α immunosensor with other techniques

Material/method	Linear Range	LOD	Ref.
C_{60}@f-MWCNTs@RTIL/DPV	0.005–0.075 ng mL^{-1}	0.002 ng mL^{-1}	[58]
Fe_3O_4@AuNPs-DNA@MagGCE/SWV	0.01–100.0 ng mL^{-1}	0.01 ng mL^{-1}	[59]
Py@Py-COOH@MagNPs@SP-AuE/AMP	0.001–0.015 ng mL^{-1}	0.3 pg mL^{-1}	[60]
CMA@AuE/AMP	0.001–0.03 ng mL^{-1}	0.001 ng mL^{-1}	[61]
HOOC-Phe-DWCNTs/SPCE	0.001–0.20 ng mL^{-1}	0.85 pg mL^{-1}	[28]
SERS	0.17 pg mL^{-1} - 0.20 μg mL^{-1}	0.17 pg mL^{-1}	[62]
QCM	0.0–100.0 pg mL^{-1}	1.62 pg mL^{-1}	[63]
SERS	1.00 pg mL^{-1} - 10.0 ng mL^{-1}	1.00 pg mL^{-1}	[64]
AuNPs@PDDA@Fc-PNW@GCE/SWV	0.005–10.0 ng mL^{-1}	0.002 ng mL^{-1}	[65]
4-ABA@SPCE/DPV	3.25–50.0 ng mL^{-1}	4.10 ng mL^{-1}	[66]
Ni/Cu-MOFs	0.01–1.0 pg mL^{-1}	2.0 fg mL^{-1}	This study

addition methods showed the high selectivity without interference effect from the other proteins.

Selectivity, stability, reproducibility, and reusability

For the selectivity test of immunosensor, seven different protein solutions including TNF-α, IL-1, IL-2, IL-4, IL-6, IL-10, and BSA were prepared and voltammetric TNF-α immunosensors were separately developed by using these 7 antigen protein solutions. Then, voltammetric TNF-α immunosensor was applied to 1.0 mM H_2O_2 solution including in pH 7.0, 0.1 M PBS (2.0 mL). According to Fig. 6A, 0.53% of relative standard deviation (RSD) showed high selectivity of voltammetric TNF-α immunosensor.

During 7 weeks, the voltammetric TNF-α immunosensors were stored at 4 °C and applied to 1.0 mM H_2O_2 solution including in pH 7.0, 0.1 M PBS (2.0 mL). The signals were about 97.83% of first current signal during 7 weeks (Fig. 6B). Hence, a novel voltammetric TNF-α immunosensor with high stability was presented for clinical applications.

For reproducibility test, 30 voltammetric TNF-α immunosensors with 0.100 pg mL^{-1} antigen TNF-α were prepared and applied to 1.0 mM H_2O_2 solution including in pH 7.0, 0.1 M PBS (2.0 mL). 0.42% of RSD demonstrated the high reliability of the immunosensor production procedure. Lastly, the reusability of voltammetric TNF-α immunosensor including 0.100 pg mL^{-1} antigen TNF-α was investigated. We constantly recorded the voltammograms' signals during 50 usage of one voltammetric TNF-α immunosensor and RSD value was calculated as 0.61%. Hence, a high degree of reusability can be mentioned for voltammetric TNF-α immunosensor in this study.

Conclusions

In this study, the selective, sensitive, stable, and reproducible new-type voltammetric immunosensor based on gold nanoparticles involved in thiol-functionalized multi-walled carbon nanotubes and bimetallic Ni/Cu-MOFs was prepared and

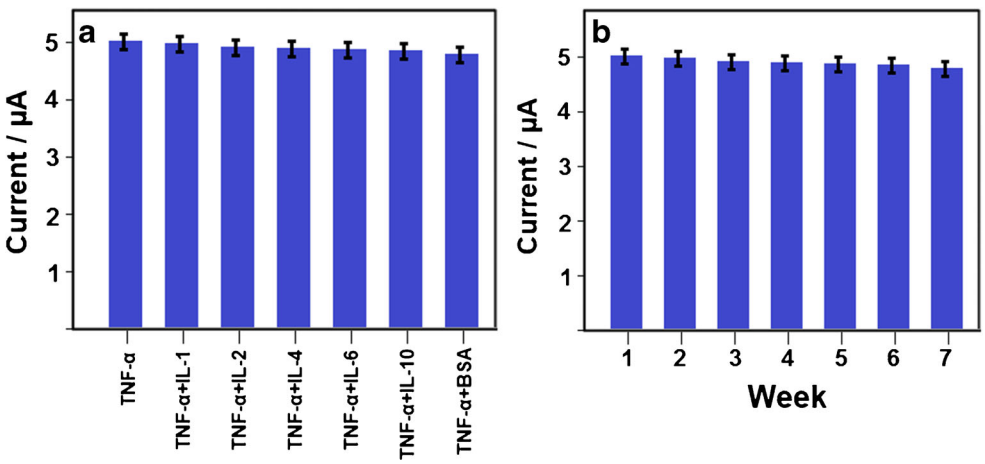

Fig. 6 (A) Immunosensor responses against the prepared solutions ($n = 6$): (i) 0.100 pg mL^{-1} TNF-α, (ii) 0.100 pg mL^{-1} TNF-α + 1.00 pg mL^{-1} IL-1, (iii) 0.100 pg mL^{-1} TNF-α + 1.00 pg mL^{-1} IL-2, (iv) 0.100 pg mL^{-1} TNF-α + 1.00 pg mL^{-1} IL-4, (v) 0.100 pg mL^{-1} TNF-α + 1.00 pg mL^{-1} IL-6, (vi) 0.100 pg mL^{-1} TNF-α + 1.00 pg mL^{-1} IL-10, (vii) 0.100 pg mL^{-1} TNF-α + 1.00 pg mL^{-1} BSA. (B) Stability test of voltammetric TNF-α immunosensors including 0.100 pg mL^{-1} antigen TNF-α ($n = 6$)

applied to tumor necrosis factor-alpha detection in plasma samples. In comparison with the other detection methods, the prepared immunosensor had more satisfactory sensitivity and showed a detection limit of 2.0 fg mL^{-1}. Moreover, owing to the easy, low-cost, and efficient preparation procedure for AuNP/S-MWCNT composite and bimetallic Ni/Cu-MOFs, an environmentally friendly immunosensor was presented in biosensor technology. Finally, a novel voltammetric tumor necrosis factor-alpha immunosensor is developed as alternative biosensor for clinical diagnosis.

Supplementary Information The online version contains supplementary material available at https://doi.org/10.1007/s00216-021-03203-z.

Acknowledgements Mehmet Lütfi Yola would like to thank Turkish Academy of Sciences (TUBA- GEBIP) for their invaluable support.

Declarations

Because free plasma samples were supplied from Hacettepe University, Blood Bank, in Turkey, an ethical approval was not necessary.

Conflict of interests The authors declare no conflict of interest.

References

1. Stenken JA, Poschenrieder AJ. Bioanalytical chemistry of cytokines – a review. Anal Chim Acta. 2015;853:95–115. https://doi.org/10.1016/j.aca.2014.10.009.
2. Liu G, Qi M, Hutchinson MR, Yang G, Goldys EM. Recent advances in cytokine detection by immunosensing. Biosens Bioelectron. 2016;79:810–21. https://doi.org/10.1016/j.bios.2016.01.020.
3. Zhang J-M, An J. Cytokines, inflammation, and pain. Int Anesthesiol Clin. 2007;45(2):27–37. https://doi.org/10.1097/AIA.0b013e318034194e.
4. Asiedu MK, Ingle JN, Behrens MD, Radisky DC, Knutson KL. TGFβ/TNFα-mediated epithelial–mesenchymal transition generates breast cancer stem cells with a claudin-low phenotype. Cancer Res. 2011;71(13):4707–19. https://doi.org/10.1158/0008-5472.can-10-4554.
5. Hotamisligil GS, Peraldi P, Budavari A, Ellis R, White MF, Spiegelman BM. IRS-1-mediated inhibition of insulin receptor tyrosine kinase activity in TNF-α- and obesity-induced insulin resistance. Science. 1996;271(5249):665–70. https://doi.org/10.1126/science.271.5249.665.
6. Ali I, Lone MN, Al-Othman ZA, Al-Warthan A, Sanagi MM. Heterocyclic scaffolds: centrality in anticancer drug development. Curr Drug Targets. 2015;16(7):711–34. https://doi.org/10.2174/1389450116666150309115922.
7. Ali I. Nano anti-cancer drugs: pros and cons and future perspectives. Curr Cancer Drug Targets. 2011;11(2):131–4. https://doi.org/10.2174/156800911794328457.
8. Ali I, Saleem K, Wesselinova D, Haque A. Synthesis, DNA binding, hemolytic, and anti-cancer assays of curcumin I-based ligands and their ruthenium (III) complexes. Med Chem Res. 2013;22(3):1386–98. https://doi.org/10.1007/s00044-012-0133-8.
9. Ali I, Lone MN, Aboul-Enein HY. Imidazoles as potential anticancer agents. Med Chem Commun. 2017;8(9):1742–73. https://doi.org/10.1039/C7MD00067G.
10. Usuba R, Yokokawa M, Ackermann TN, Llobera A, Fukunaga K, Murata S, et al. Photonic lab-on-a-chip for rapid cytokine detection. ACS Sens. 2016;1(8):979–86. https://doi.org/10.1021/acssensors.6b00193.
11. Chiswick EL, Duffy E, Japp B, Remick D. Detection and quantification of cytokines and other biomarkers. Methods Mol Biol. 2012;844:15–30. https://doi.org/10.1007/978-1-61779-527-5_2.
12. Cox JH, Ferrari G, Janetzki S. Measurement of cytokine release at the single cell level using the ELISPOT assay. Methods. 2006;38(4):274–82. https://doi.org/10.1016/j.ymeth.2005.11.006.
13. Schröder C, Jacob A, Tonack S, Radon TP, Sill M, Zucknick M, et al. Dual-color proteomic profiling of complex samples with a microarray of 810 cancer-related antibodies. Mol Cell Proteomics. 2010;9(6):1271–80. https://doi.org/10.1074/mcp.M900419-MCP200.
14. Campos LA, Liu J, Wang X, Ramanathan R, English DS, Muñoz V. A photoprotection strategy for microsecond-resolution single-molecule fluorescence spectroscopy. Nat Methods. 2011;8(2):143–6. https://doi.org/10.1038/nmeth.1553.
15. Mayer KM, Hafner JH. Localized surface plasmon resonance sensors. Chem Rev. 2011;111(6):3828–57. https://doi.org/10.1021/cr100313v.
16. Filik H, Avan AA. Electrochemical immunosensors for the detection of cytokine tumor necrosis factor alpha: a review. Talanta. 2020;211:120758. https://doi.org/10.1016/j.talanta.2020.120758.
17. Oh B-R, Huang N-T, Chen W, Seo JH, Chen P, Cornell TT, et al. Integrated nanoplasmonic sensing for cellular functional immunoanalysis using human blood. ACS Nano. 2014;8(3):2667–76. https://doi.org/10.1021/nn406370u.
18. Jeong H-H, Erdene N, Park J-H, Jeong D-H, Lee H-Y, Lee S-K. Real-time label-free immunoassay of interferon-gamma and prostate-specific antigen using a fiber-optic localized surface plasmon resonance sensor. Biosens Bioelectron. 2013;39(1):346–51. https://doi.org/10.1016/j.bios.2012.08.013.
19. Luo X, Davis JJ. Electrical biosensors and the label free detection of protein disease biomarkers. Chem Soc Rev. 2013;42(13):5944–62. https://doi.org/10.1039/C3CS60077G.
20. Karimi-Maleh H, Arotiba OA. Simultaneous determination of cholesterol, ascorbic acid and uric acid as three essential biological compounds at a carbon paste electrode modified with copper oxide decorated reduced graphene oxide nanocomposite and ionic liquid. J Colloid Interface Sci. 2020;560:208–12. https://doi.org/10.1016/j.jcis.2019.10.007.
21. Karimi-Maleh H, Karimi F, Alizadeh M, Sanati AL. Electrochemical sensors, a bright future in the fabrication of portable kits in analytical systems. Chem Rec. 2020;20(7):682–92. https://doi.org/10.1002/tcr.201900092.
22. Tahernejad-Javazmi F, Shabani-Nooshabadi M, Karimi-Maleh H. 3D reduced graphene oxide/FeNi3-ionic liquid nanocomposite modified sensor; an electrical synergic effect for development of tert-butylhydroquinone and folic acid sensor. Compos Part B. 2019;172:666–70. https://doi.org/10.1016/j.compositesb.2019.05.065.
23. Miraki M, Karimi-Maleh H, Taher MA, Cheraghi S, Karimi F, Agarwal S, et al. Voltammetric amplified platform based on ionic liquid/NiO nanocomposite for determination of benserazide and levodopa. J Mol Liq. 2019;278:672–6. https://doi.org/10.1016/j.molliq.2019.01.081.
24. Karimi-Maleh H, Sheikhshoaie M, Sheikhshoaie I, Ranjbar M, Alizadeh J, Maxakato NW, et al. A novel electrochemical epinine sensor using amplified CuO nanoparticles and a n-hexyl-3-methylimidazolium hexafluorophosphate electrode. New J Chem. 2019;43(5):2362–7. https://doi.org/10.1039/C8NJ05581E.
25. Medetalibeyoglu H, Beytur M, Akyıldırım O, Atar N, Yola ML. Validated electrochemical immunosensor for ultra-sensitive procalcitonin detection: carbon electrode modified with gold

nanoparticles functionalized sulfur doped MXene as sensor platform and carboxylated graphitic carbon nitride as signal amplification. Sensors Actuators B Chem. 2020;319:128195. https://doi.org/10.1016/j.snb.2020.128195.
26. Yola ML, Atar N. Amperometric galectin-3 immunosensor-based gold nanoparticle-functionalized graphitic carbon nitride nanosheets and core–shell Ti-MOF@COFs composites. Nanoscale. 2020;12(38):19824–32. https://doi.org/10.1039/D0NR05614F.
27. Yuan L, Hua X, Wu Y, Pan X, Liu S. Polymer-functionalized silica nanosphere labels for ultrasensitive detection of tumor necrosis factor-alpha. Anal Chem. 2011;83(17):6800–9. https://doi.org/10.1021/ac201558w.
28. Sánchez-Tirado E, Salvo C, González-Cortés A, Yáñez-Sedeño P, Langa F, Pingarrón JM. Electrochemical immunosensor for simultaneous determination of interleukin-1 beta and tumor necrosis factor alpha in serum and saliva using dual screen printed electrodes modified with functionalized double–walled carbon nanotubes. Anal Chim Acta. 2017;959:66–73. https://doi.org/10.1016/j.aca.2016.12.034.
29. Ajayan PM. Nanotubes from carbon. Chem Rev. 1999;99(7):1787–800. https://doi.org/10.1021/cr970102g.
30. Britto PJ, Santhanam KSV, Rubio A, Alonso JA, Ajayan PM. Improved charge transfer at carbon nanotube electrodes. Adv Mater. 1999;11(2):154–7. https://doi.org/10.1002/(sici)1521-4095(199902)11:2<154::aid-adma154>3.0.co;2-b.
31. Kolahi-Ahari S, Deiminiat B, Rounaghi GH. Modification of a pencil graphite electrode with multiwalled carbon nanotubes capped gold nanoparticles for electrochemical determination of tramadol. J Electroanal Chem. 2020;862:113996. https://doi.org/10.1016/j.jelechem.2020.113996.
32. Liao X, Fu H, Yan T, Lei J. Electroactive metal-organic framework composites: design and biosensing application. Biosens Bioelectron. 2019;146:111743. https://doi.org/10.1016/j.bios.2019.111743.
33. Zhou H, Zheng M, Tang H, Xu B, Tang Y, Pang H. Amorphous intermediate derivative from ZIF-67 and its outstanding electrocatalytic activity. Small. 2020;16(2):1904252. https://doi.org/10.1002/smll.201904252.
34. Abuzalat O, Wong D, Park SS, Kim S. Highly selective and sensitive fluorescent zeolitic imidazole frameworks sensor for nitroaromatic explosive detection. Nanoscale. 2020;12(25):13523–30. https://doi.org/10.1039/D0NR01653E.
35. Jian X, Xu J, Yang L, Zhao C, Xu J, Gao Z, et al. Intracellular metal-organic frameworks: integrating an all-in-one semiconductor electrode chip for therapy, capture, and quantification of circulating tumor cells. Anal Chem. 2020;92(19):13319–26. https://doi.org/10.1021/acs.analchem.0c02618.
36. Guo J, Yang L, Gao Z, Zhao C, Mei Y, Song Y-Y. Insight of MOF environment-dependent enzyme activity via MOFs-in-nanochannels configuration. ACS Catal. 2020;10:5949–58. https://doi.org/10.1021/acscatal.0c00591.
37. Chen J, Xu Q, Shu Y, Hu X. Synthesis of a novel Au nanoparticles decorated Ni-MOF/Ni/NiO nanocomposite and electrocatalytic performance for the detection of glucose in human serum. Talanta. 2018;184:136–42. https://doi.org/10.1016/j.talanta.2018.02.057.
38. Yang J, Yang Y-W. Metal–organic frameworks for biomedical applications. Small. 2020;16(10):1906846. https://doi.org/10.1002/smll.201906846.
39. Zhou W, Huang D-D, Wu Y-P, Zhao J, Wu T, Zhang J, et al. Stable hierarchical bimetal–organic nanostructures as high performance electrocatalysts for the oxygen evolution reaction. Angew Chem Int Ed. 2019;58(13):4227–31. https://doi.org/10.1002/anie.201813634.
40. Fang G, Wang Q, Zhou J, Lei Y, Chen Z, Wang Z, et al. Metal organic framework-templated synthesis of bimetallic selenides with rich phase boundaries for sodium-ion storage and oxygen evolution reaction. ACS Nano. 2019;13(5):5635–45. https://doi.org/10.1021/acsnano.9b00816.
41. Janegitz BC, Pauliukaite R, Ghica ME, Brett CMA, Fatibello-Filho O. Direct electron transfer of glucose oxidase at glassy carbon electrode modified with functionalized carbon nanotubes within a dihexadecylphosphate film. Sensors Actuators B Chem. 2011;158(1):411–7. https://doi.org/10.1016/j.snb.2011.06.048.
42. Yola ML, Atar N. A novel voltammetric sensor based on gold nanoparticles involved in p-aminothiophenol functionalized multi-walled carbon nanotubes: application to the simultaneous determination of quercetin and rutin. Electrochim Acta. 2014;119:24–31. https://doi.org/10.1016/j.electacta.2013.12.028.
43. Glišić BĐ, Rychlewska U, Djuran MI. Reactions and structural characterization of gold (iii) complexes with amino acids, peptides and proteins. Dalton Trans. 2012;41(23):6887–901. https://doi.org/10.1039/C2DT30169E.
44. La Belle JT, Demirok UK, Patel DR, Cook CB. Development of a novel single sensor multiplexed marker assay. Analyst. 2011;136(7):1496–501. https://doi.org/10.1039/C0AN00923G.
45. Zhou N, Ma Y, Hu B, He L, Wang S, Zhang Z, et al. Construction of Ce-MOF@COF hybrid nanostructure: label-free aptasensor for the ultrasensitive detection of oxytetracycline residues in aqueous solution environments. Biosens Bioelectron. 2019;127:92–100. https://doi.org/10.1016/j.bios.2018.12.024.
46. Stanković V, Đurđić S, Ognjanović M, Mutić J, Kalcher K, Stanković DM. A novel nonenzymatic hydrogen peroxide amperometric sensor based on AgNp@GNR nanocomposites modified screen-printed carbon electrode. J Electroanal Chem. 2020;876:114487. https://doi.org/10.1016/j.jelechem.2020.114487.
47. Yola ML, Atar N. Development of cardiac troponin-I biosensor based on boron nitride quantum dots including molecularly imprinted polymer. Biosens Bioelectron. 2019;126:418–24. https://doi.org/10.1016/j.bios.2018.11.016.
48. Wang S, Wang M, Li C, Li H, Ge C, Zhang X, et al. A highly sensitive and stable electrochemiluminescence immunosensor for alpha-fetoprotein detection based on luminol-AgNPs@Co/Ni-MOF nanosheet microflowers. Sensors Actuators B Chem. 2020;311:127919. https://doi.org/10.1016/j.snb.2020.127919.
49. Yang J, Zheng C, Xiong P, Li Y, Wei M. Zn-doped Ni-MOF material with a high supercapacitive performance. J Mater Chem A. 2014;2(44):19005–10. https://doi.org/10.1039/C4TA04346D.
50. Yola ML, Atar N, Üstündağ Z, Solak AO. A novel voltammetric sensor based on p-aminothiophenol functionalized graphene oxide/gold nanoparticles for determining quercetin in the presence of ascorbic acid. J Electroanal Chem. 2013;698:9–16. https://doi.org/10.1016/j.jelechem.2013.03.016.
51. Gupta VK, Yola ML, Qureshi MS, Solak AO, Atar N, Üstündağ Z. A novel impedimetric biosensor based on graphene oxide/gold nanoplatform for detection of DNA arrays. Sensors Actuators B Chem. 2013;188:1201–11. https://doi.org/10.1016/j.snb.2013.08.034.
52. Ahmadpoor F, Zebarjad SM, Janghorban K. Decoration of multi-walled carbon nanotubes with silver nanoparticles and investigation on its colloid stability. Mater Chem Phys. 2013;139(1):113–7. https://doi.org/10.1016/j.matchemphys.2012.12.071.
53. Sheberla D, Sun L, Blood-Forsythe MA, Er S, Wade CR, Brozek CK, et al. High electrical conductivity in Ni3(2,3,6,7,10,11-hexaiminotriphenylene)2, a semiconducting metal–organic graphene analogue. J Am Chem Soc. 2014;136(25):8859–62. https://doi.org/10.1021/ja502765n.
54. Campbell MG, Sheberla D, Liu SF, Swager TM, Dincă M. Cu3(hexaiminotriphenylene)2: an electrically conductive 2D metal–organic framework for chemiresistive sensing. Angew Chem Int Ed. 2015;54(14):4349–52. https://doi.org/10.1002/anie.201411854.

55. Lou X, Ning Y, Li C, Hu X, Shen M, Hu B. Bimetallic zeolite imidazolate framework for enhanced lithium storage boosted by the redox participation of nitrogen atoms. Sci China Mater. 2018;61(8):1040–8. https://doi.org/10.1007/s40843-017-9200-5.
56. Wang Z, Li M, Zhang Y, Yuan J, Shen Y, Niu L, et al. Thionine-interlinked multi-walled carbon nanotube/gold nanoparticle composites. Carbon. 2007;45(10):2111–5. https://doi.org/10.1016/j.carbon.2007.05.018.
57. Mattioli IA, Baccarin M, Cervini P, Cavalheiro ÉTG. Electrochemical investigation of a graphite-polyurethane composite electrode modified with electrodeposited gold nanoparticles in the voltammetric determination of tryptophan. J Electroanal Chem. 2019;835:212–9. https://doi.org/10.1016/j.jelechem.2018.12.056.
58. Mazloum-Ardakani M, Hosseinzadeh L, Khoshroo A. Label-free electrochemical immunosensor for detection of tumor necrosis factor α based on fullerene-functionalized carbon nanotubes/ionic liquid. J Electroanal Chem. 2015;757:58–64. https://doi.org/10.1016/j.jelechem.2015.09.006.
59. Miao P, Yang D, Chen X, Guo Z, Tang Y. Voltammetric determination of tumor necrosis factor-α based on the use of an aptamer and magnetic nanoparticles loaded with gold nanoparticles. Microchim Acta. 2017;184(10):3901–7. https://doi.org/10.1007/s00604-017-2419-5.
60. Barhoumi L, Bellagambi FG, Vivaldi FM, Baraket A, Clément Y, Zine N, et al. Ultrasensitive immunosensor array for TNF-α detection in artificial saliva using polymer-coated magnetic microparticles onto screen-printed gold electrode. Sensors. 2019;19(3):692. https://doi.org/10.3390/s19030692.
61. Barhoumi L, Baraket A, Bellagambi FG, Karanasiou GS, Ali MB, Fotiadis DI, et al. A novel chronoamperometric immunosensor for rapid detection of TNF-α in human saliva. Sensors Actuators B Chem. 2018;266:477–84. https://doi.org/10.1016/j.snb.2018.03.135.
62. Gholami MD, Sonar P, Ayoko GA, Izake EL. A highly sensitive SERS quenching nanosensor for the determination of tumor necrosis factor alpha in blood. Sensors Actuators B Chem. 2020;310:127867. https://doi.org/10.1016/j.snb.2020.127867.
63. Pohanka M. Piezoelectric biosensor for the determination of tumor necrosis factor alpha. Talanta. 2018;178:970–3. https://doi.org/10.1016/j.talanta.2017.10.031.
64. Lai Y, Schlücker S, Wang Y. Rapid and sensitive SERS detection of the cytokine tumor necrosis factor alpha (tnf-α) in a magnetic bead pull-down assay with purified and highly Raman-active gold nanoparticle clusters. Anal Bioanal Chem. 2018;410(23):5993–6000. https://doi.org/10.1007/s00216-018-1218-0.
65. Sun Z, Deng L, Gan H, Shen R, Yang M, Zhang Y. Sensitive immunosensor for tumor necrosis factor α based on dual signal amplification of ferrocene modified self-assembled peptide nanowire and glucose oxidase functionalized gold nanorod. Biosens Bioelectron. 2013;39(1):215–9. https://doi.org/10.1016/j.bios.2012.07.050.
66. Eletxigerra U, Martinez-Perdiguero J, Merino S. Disposable microfluidic immuno-biochip for rapid electrochemical detection of tumor necrosis factor alpha biomarker. Sensors Actuators B Chem. 2015;221:1406–11. https://doi.org/10.1016/j.snb.2015.08.026.